Check for updates

Single component white-OLEDs derived from tris(β-diketonato) europium(III) complexes bearing the large bite angle N^N 2-(4-thiazolyl)benzimidazole ligand†

Rashid Ilmi, [ID] *[a] Jiaxuan Yin,[b] José D. L. Dutra, [ID] [c] Nawal K. Al Rasbi, [ID] [a] Willyan F. Oliveira,[c] Liang Zhou, [ID] *[b] Wai-Yeung Wong, [ID] *[d] Paul R. Raithby [ID] *[e] and Muhammad S. Khan [ID] *[a]

Two new organo-europium complexes (OEuCs) [Eu(tfac)$_3$(TB-Im)] (**Eu1**) [Eu(hfac)$_3$(TB-Im)] (**Eu2**) incorporating fluorinated (hexafluoroacetylacetone; Hhfaa) or hemi-fluorinated (trifluoroacetylacetone; Htfac) β-diketones together with the large bite angle N^N ligand (2-(4-thiazolyl)benzimidazole; TB-Im) have been synthesized and characterized. The structure of the complexes has been established by single crystal X-ray diffraction (SC-XRD) analysis and shows that the coordination sphere is composed of a EuO$_6$N$_2$ core (octacoordinated). Continuous shape measures (CShMs) revealed that the geometry around Eu(III) is trigonal dodecahedral with approximate D_{2d}-symmetry. Efficient red emission is observed for both the complexes in solution with a fairly large photoluminescence quantum yield (PLQY (Q_{Eu}^L) = 39.00–47.00%). Furthermore, by utilizing the experimental photoluminescence (PL) data and theoretical modelling employing density functional theory (DFT) in conjunction with LUMPAC, energy transfer (ET) and back energy transfer rates were calculated, and an ET mechanism for the sensitized PL is proposed and discussed in detail. Finally, the complexes were used as an emitting layer (EML) to fabricate 20 organic light emitting diodes (OLEDs) by varying the doping concentration. Interestingly, both the complex-based OLEDs at 4 wt% doping concentration display white electroluminescence (EL) with the brightness (B) = 100.5–364.1 cd m^{-2} at very low turn-on voltage ($V_{\text{turn-on}}$) = 3.9–4.6 V. The overall electroluminescence performance of **Eu1** and **Eu2** is higher than that of the reported europium based single component white-OLEDs.

[a]*Department of Chemistry, Sultan Qaboos University, P. O. Box 36, Al Khod 123, Oman. E-mail: rashidilmi@gmail.com, msk@squ.edu.om*
[b]*State Key Laboratory of Rare Earth Resource Utilization, Changchun Institute of Applied Chemistry, Chinese Academy of Sciences, Renmin Street 5625, Changchun 130022, People's Republic of China. E-mail: zhoul@ciac.ac.cn*
[c]*Pople Computational Chemistry Laboratory, Department of Chemistry, UFS, 49100-000 São Cristóvão, Sergipe, Brazil*
[d]*Department of Applied Biology and Chemical Technology, The Hong Kong Polytechnic University, Hung Hom, Kowloon, Hong Kong, People's Republic of China. E-mail: wai-yeung.wong@polyu.edu.hk*
[e]*Department of Chemistry, University of Bath, Claverton Down, Bath, BA2 7AY, UK. E-mail: p.r.raithby@bath.ac.uk*
†Electronic supplementary information (ESI) available. CCDC 2178685 and 2178686. For ESI and crystallographic data in CIF or other electronic format see DOI: https://doi.org/10.1039/d2dt01873j

1. Introduction

Research into the design and development of coordination complexes capable of panchromatic emission either in their molecular forms or in devices has received considerable attention.[1] This is because of their wide application in full-colour flat-panel displays and solid-state lighting for the benefit of energy conservation.[2] One of the promising classes of complexes for further development is the class of efficient organo-europium complexes (OEuCs) because of their exemplary photophysical properties leading to many fascinating applications such as sensors[3] and thermometers,[4] and in anti-counterfeiting applications.[5] To develop efficient OEuCs, the organic ligand(s) acting either as the primary antenna or as the ancillary ligands must have strong light absorption capabilities between 250 and 450 nm with a compatible triplet state ($^3\pi\pi^*$) leading to sufficiently separated $^3\pi\pi^*$ and Eu(III) emitting levels.[6] This allows efficient harvesting of the absorbed energy by the organic ligand(s) through the well-known antenna effect.[7] Besides, the intrinsic monochromatic red emission due to the electric-dipole (ED) $^5D_0 \rightarrow {}^7F_2$ transition of Eu(III)[8] between 608 nm and 620 nm makes these complexes potential candidates as the red component[9] to fabricate tricolour RGB-based

white organic light emitting diodes (white-OLEDs) given that the OEuCs exhibit efficient PL properties.

As simple as it sounds, the generation of white light *i.e.*, panchromatic emission in any phase (crystal/solution/film) remains challenging if a three-component approach is used and has some serious drawbacks *e.g.*, colour impurity as the device ages, manufacturing cost as well as labour to fabricate them, thereby impeding their real-life and industrial applications.[1b,10] To overcome these issues, the development of energy-efficient white-OLEDs from a single molecular platform could provide an elegant solution.[1b] Among the different strategies, an appropriate way to achieve white light emission from a single compound is the generation of blue and reddish-orange emissions concomitantly.[10] Interestingly, OEuCs could be employed as EMLs to fabricate white-OLEDs particularly because they display three emission transitions in the reddish-orange region also because they have microsecond to milli-second excited state lifetimes. It is well known that as the current density increases, the longer excited lifetime decays non-radiatively due to triplet–triplet annihilation[11] leading to emissions in the region between 400 and 500 nm.
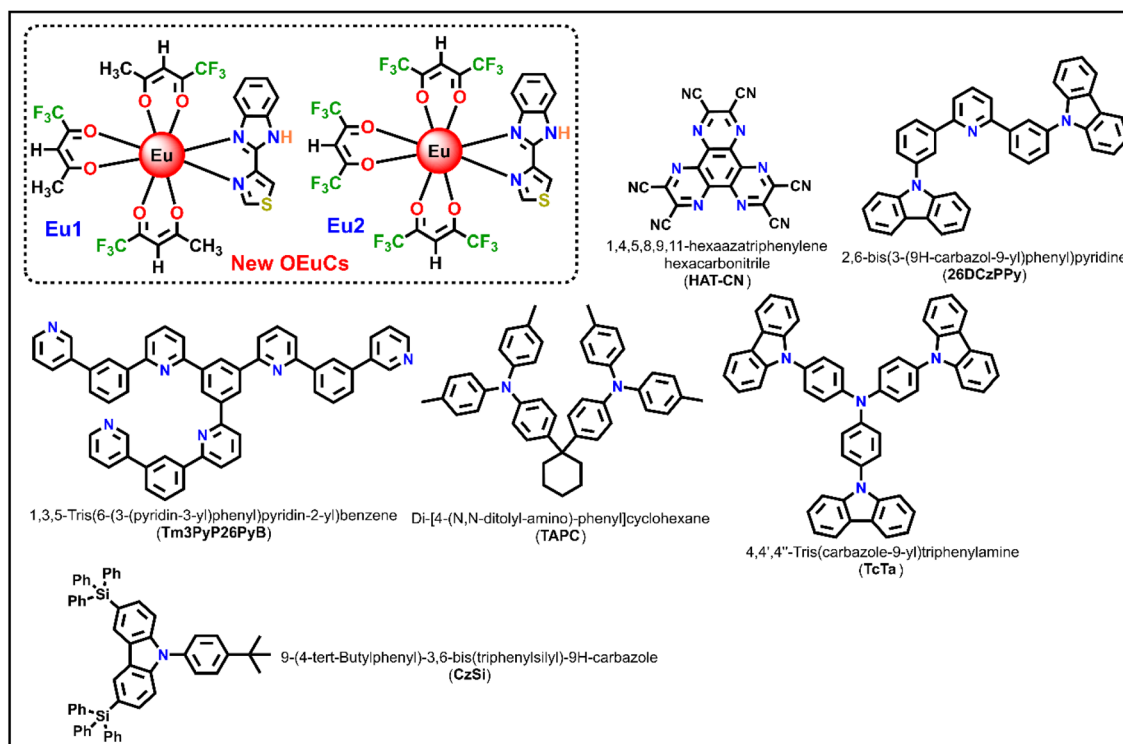
Keeping this idea in mind, in the present work, we synthesized two new OEuCs complexes (Chart 1) by employing hemi-fluorinated (Htfac) and fluorinated (Hhfac) acetylace-tones as the primary antenna ligands in conjunction with TB-Im as an ancillary ligand. It is well established that both the β-diketones act as efficient antenna ligands to generate highly luminescent OEuCs,[1b,d,12] which is attributed to the well-placed $^3\pi\pi^*$ ($^3\pi\pi^*$ = 22 720 cm^{-1} for tfac and 21 930 cm^{-1}

for hfac) transitions fulfilling Latva's empirical rule.[6b] The bidentate ancillary TB-Im ligand was chosen because of the asymmetrical N^N-chelating coordination mode *via* the five-membered imidazolyl ring fused with phenyl ring (benzoimi-dazole ring C–N = 1.393 Å) and five-membered thiazolyl ring (C–N = 1.295 Å). As noted by us and others, large bite angle coordinating ligands have a profound effect in distorting the coordination geometry around the Ln(III) centre, which is ben-eficial for enhancing the PL properties.[9a,c,13] Besides, the NH proton of the imidazolyl ring is often engaged in the formation of intermolecular hydrogen bonds leading to supramolecular self-assembly, that result in fascinating structural arrange-ments in the solid-state.[1a] We now present the details of the synthesis of **Eu1** and **Eu2**, (Chart 1), their structural character-isation, and their photophysical properties. The results are supported by theoretical studies and an ET mechanism of the sensitized emission for the OEuCs is proposed. Finally, we have employed **Eu1** and **Eu2** as an emitter to fabricate single- and double-EML OLEDs.

2. Experimental

2.1. Synthesis of the complexes

Eu(III) chloride was purchased from Strem Chemicals, Inc. Htfac, Hhfac and TB-Im were obtained from Tokyo Chemical Industry (TCI) and were used as received. Solvents were pre-dried and distilled before use according to standard pro-cedures. All organic compounds employed in OLED fabrica-

Chart 1 Chemical structures of new OEuCs and organic compounds employed in the OLEDs fabrication.

tion were procured from commercial sources and used without further purification unless otherwise specified (Chart 1). Elemental analysis was performed on an Euro EA – CHN in the Department of Chemistry, Sultan Qaboos University. Attenuated total-reflectance (ATR) infrared (IR) spectra were recorded on pure samples on diamond using a Cary 630 F T-IR spectrometer. Mass spectra were obtained using LCMS-8040, Shimazdu-Japan coupled to a triple quadruple tandem mass spectrometer equipped with electrospray ionization (ESI). The thermal stability of the complexes was determined by thermogravimetric analysis (TGA) and differential thermogravimetric analysis (DTA) in the temperature range between 50 and 700 °C under a dinitrogen (N_2) atmosphere and recorded on TA instrument model SDTQ600.

2.1.1.   [Eu(tfac)$_3$(TB-Im)] (Eu1). Eu-1 was synthesized by reacting equimolar quantities of [Eu(tfac)$_3$(H$_2$O)$_2$][1b] (0.5 g; 0.771 mmol) and TB-Im (0.155 g; 0.771 mmol) in 1 : 1 mixture of dichloromethane (DCM) and ethanol (EtOH). The reaction mixture was stirred overnight at room temperature and left for slow solvent evaporation. After a week crystals suitable for single-crystal X-ray analysis were obtained. Colour: white; yield (70%); microanalysis calculated for $C_{25}H_{19}EuF_9N_3O_6S$: C, 36.96; H, 2.36; N, 5.17; found: C, 36.98; H, 2.34; N, 5.16; FTIR (solid; cm^{-1})- ν(N–H) 3251 cm^{-1}; ν(C=O)$_{st}$ 1617 cm^{-1}; ν(C=N)$_{st}$ 1524 cm^{-1}; out-of plane asymmetric ν(C–F)$_{st}$ 1177 cm^{-1}; in-plane ν(C–H)$_{bend.}$ 1124 cm^{-1}, (Fig. S1, ESI†); ESI-MS (m/z) = 812.1 [M + H] (Fig. S2, ESI†) melting temperature (T_m) = 228.9 °C decomposition temperature (T_d) with 5% weight loss = 241 °C.

2.1.2.   [Eu(hfac)$_3$(TB-Im)] (Eu2). Eu2 was synthesized using a one-pot method reported earlier for the synthesis of related complexes.[1d] Colour: white; yield (68%); microanalysis calculated for $C_{25}H_{10}EuF_{18}N_3O_6S$: C, 30.82; H, 1.03; N, 4.31; found: C, 30.84; H, 0.99; N, 4.29; FT-IR (solid; cm^{-1})- ν(N–H) 3297 cm^{-1}; ν(C–O)$_{st}$ 1642 cm^{-1}; ν(C=N)$_{st}$ 1531 cm^{-1}; out-of plane asymmetric ν(C–F)$_{st}$ 1194 cm^{-1}; in-plane ν(C–H)$_{bend.}$ 1137 cm^{-1}; (Fig. S3, ESI†); ESI-MS (m/z) = 1013.20 [M + K − 2H] (Fig. S4, ESI†); T_m = 202 °C, T_d with 5% weight loss = 239 °C.

2.2.   Single crystal X-ray structure determination

Single crystals of **Eu1** and **Eu2** suitable for single-crystal X-ray analysis were grown by the slow solvent (EtOH) evaporation method. The structure determination was performed at room temperature on a Stoe IPS II diffractometer using monochromatic Mo-Kα radiation (λ = 0.71073 Å). A multi-scan absorption correction was applied. The data reduction, including an empirical absorption correction using spherical harmonics, was implemented in LANA. The crystal structure was solved by direct methods using the online version of WinGX[14] and then refined by full-matrix least-squares (SHELXL-2018) on F^2.[15] The non-hydrogen atoms were refined anisotropically. All of the hydrogen atoms were positioned geometrically in idealized positions and refined with the riding model approximation, with $U_{iso}(H) = 1.2U_{eq}(C)$. The displacement ellipsoids particularly on the fluorine atoms of the CF_3 groups were elongated because of disorder however they could be modelled appropri-

ately using a single atom position for each fluorine atom. Crystal data and structure refinement for europium complexes are detailed in Table S2, ESI.† The molecular graphics were produced using the program MERCURY from the CSD package.[16]

2.3.   Spectroscopic measurements and OLED fabrication process

Spectroscopic measurements of the complexes that include optical absorption, excitation, emission spectra, decay profiles and absolute PLQY values were performed at room temperature; the methodology for the measurements have been reported previously.[9c] Optical absorption spectra were obtained using Varian Cary 5000 UV-Visible-NIR spectrophotometer while excitation, emission spectra and decay profiles were recorded on an Edinburgh FS5 fluorimeter. The absolute PLQY were determined using a calibrated integrating sphere on a C-9920-02 from the Hamamatsu Photonic instrument. Theoretical methodology details (section 1, ESI†) involving the calculation of ground-state geometry, ET rates, radiative emission rate (A_{Rad}) and theoretical PLQY are detailed in the ESI.† Important experimental photophysical parameters were calculated by the following equations as detailed in our previous reports:[1d,17]

$$\Omega_\lambda^{exp} = \frac{3\hbar A_{Rad}\left[^5D_0 \to {}^7F_J\right]}{32e^2\pi^3\chi\nu\left[^5D_0 \to {}^7F_J\right]^3\left|\left\langle {}^5D_0\|U^{(\lambda)}\|{}^7F_J\right\rangle\right|^2} \quad (1)$$

$$A_{Rad} = \sum_{J=0}^4 A_R\left[^5D_0 \to {}^7F_J\right] \quad (2)$$

$$A_{Rad}\left[^5D_0 \to {}^7F_J\right] = \frac{\nu\left[^5D_0 \to {}^7F_1\right]}{\nu\left[^5D_0 \to {}^7F_J\right]} \times \frac{A\left[^5D_0 \to {}^7F_J\right]}{A\left[^5D_0 \to {}^7F_1\right]}A_R\left[^5D_0 \to {}^7F_1\right] \quad (3)$$

$$A_{tot} = \frac{1}{\tau_{obs}} = A_{Rad} + A_{NRad} \quad (4)$$

$$\tau_{rad} = \frac{1}{A_{Rad}} \quad (5)$$

$$Q_{Eu}^{Eu} = \frac{\tau_{obs}}{\tau_{RAD}} = \frac{A_{Rad}}{A_{Rad} + A_{NRad}} \quad (6)$$

$$\eta_{sen} = \frac{Q_{Eu}^L}{Q_{Eu}^{Eu}} \quad (7)$$

ITO coated glass with the sheet resistance of 10 Ω sq^{-1} was used as the anode substrate. Prior to film deposition, patterned ITO substrates were cleaned with detergent, rinsed in de-ionized water, and finally dried in an oven. All organic layers were deposited at a rate of 0.1 nm s^{-1} under a high vacuum (≤3.0 × 10^{-5} Pa). The doped EMLs were prepared by co-evaporating dopant and host material from two sources, and the doping concentration was modulated by controlling the evaporation rate of the dopant. LiF and Al were deposited in another vacuum chamber (≤8.0 × 10^{-5} Pa) at rates of 0.01

and 1.0 nm s^{-1}, respectively, without being exposed to the atmosphere. The thicknesses of these deposited layers and the evaporation rate of individual materials were monitored in vacuum with quartz crystal monitors. A shadow mask was used to define the cathode and make eight emitting dots with an active area of 9 mm^2 on each substrate. Current density (*J*)–brightness (*B*)–voltage (*V*) characteristics were measured by using a programmable brightness light distribution characteristics measurement system C9920-11 from the Hamamatsu Photonic instrument. PL and EL spectra were measured with a calibrated Hitachi F-7000 fluorescence spectrophotometer and an Ocean Optics spectrophotometer.

3.   Results and discussion

3.1.   Synthesis, characterization and X-ray diffraction studies
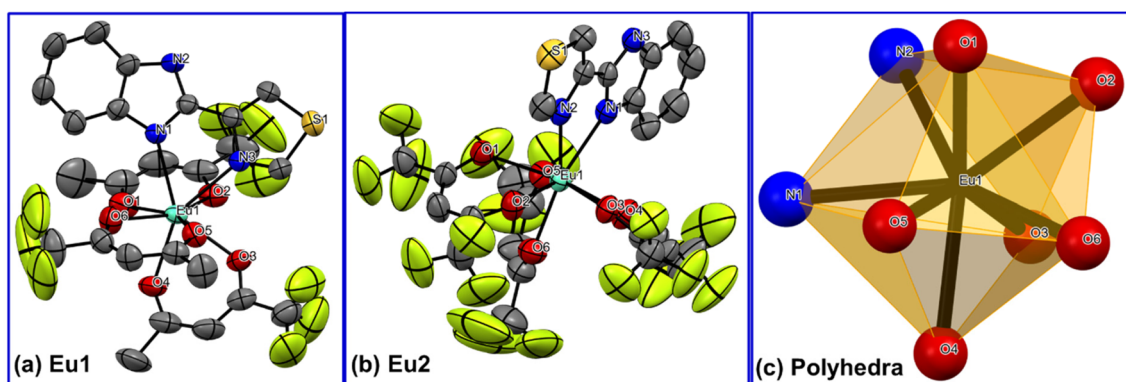
The new complexes were synthesized by the method reported earlier[1b,d] and characterized by elemental analysis, mass spectrometry and FT-IR spectroscopy. The results suggested the formation of the complexes with the formulae [Eu(tfac)$_3$(TB-Im)] (**Eu1**) [Eu(hfac)$_3$(TB-Im)] (**Eu2**). These results were confirmed by the single-crystal X-ray diffraction studies. The X-ray crystallographic data for **Eu1** and **Eu2** are given in Table S2, ESI.† The complex **Eu1** crystallizes in the triclinic space group $P\bar{1}$ while **Eu2** in monoclinic space group $P2_1/n$. The asymmetric unit in both cases consists of a single mononuclear complex in which the Eu(III) ion is eight coordinate comprising six oxygen (O) atoms from the primary β-diketone ligands and two nitrogen (N) atoms of ancillary ligands *i.e.*, N$_2$O$_6$, Fig. 1. The bond distances (Table 1) are comparable to the analogous OEuCs reported by us.[1d,9b] The Eu–N bond distances [(2.560(3) Å)$_{avg.}$ for **Eu1** and (2.554(4) Å)$_{avg.}$ for **Eu2**] are, in both cases, longer than Eu–O bond distances [(2.365(3) Å)$_{avg}$ for **Eu1** and (2.382(3) Å)$_{avg.}$ for **Eu2**] (Table 1). The coordination geometry and assignment of symmetry around the Eu(III) centres of the complexes were determined by the SHAPE software package which calculates continuous shape measures (CShMs) of a set of atomic positions relative to the vertices of ideal reference polyhedra.[18] The EuN$_2$O$_6$ coordination polyhedron can be assigned as a distorted triangular dodecahedron, with idealized D_{2d} symmetry around the metal centre (Fig. 1c). Comparison between the two structures revealed that the distortion is similar with CShM values 0.629 and 0.695 for **Eu1** and **Eu2** (Table S3, ESI†), respectively, despite the primary antenna ligand (hfac) in the latter being symmetrical.

To underpin the analysis of the photophysical properties through theoretical calculations, it is necessary to determine the ground state geometry of the complex in question. The ground state geometry of the complexes (**Eu1** and **Eu2**) was optimized from the crystallographic coordinates (details are included in the ESI† and the optimized structure is shown in Fig. S5, ESI†). The comparison involving the crystallographic geometry and the geometries calculated by different DFT methods in terms of root mean square deviations (RMSD) is

Table 1   Selected bond lengths [Å] and angles [°] for **Eu1** and **Eu2**

Eu1

Eu(1)–O(6)	2.353(3)	Eu(1)–O(3)	2.386(3)
Eu(1)–O(4)	2.354(3)	Eu(1)–O(1)	2.392(3)
Eu(1)–O(5)	2.357(3)	Eu(1)–N(1)	2.542(3)
Eu(1)–O(2)	2.385(3)	Eu(1)–N(3)	2.606(3)
O(6)–Eu(1)–O(4)	76.76(14)	O(3)–Eu(1)–O(1)	124.98(13)
O(6)–Eu(1)–O(5)	72.10(12)	O(6)–Eu(1)–N(1)	80.85(12)
O(4)–Eu(1)–O(5)	90.55(12)	O(4)–Eu(1)–N(1)	146.82(12)
O(6)–Eu(1)–O(2)	149.60(12)	O(5)–Eu(1)–N(1)	105.55(11)
O(4)–Eu(1)–O(2)	101.95(13)	O(1)–Eu(1)–N(3)	127.79(12)
O(5)–Eu(1)–O(2)	138.07(12)	N(1)–Eu(1)–N(3)	64.26(11)

Eu2

Eu(1)–O(3)	2.320(3)	Eu(1)–O(2)	2.413(3)
Eu(1)–O(6)	2.345(4)	Eu(1)–O(1)	2.444(3)
Eu(1)–O(4)	2.381(3)	Eu(1)–N(1)	2.508(4)
Eu(1)–O(5)	2.394(4)	Eu(1)–N(2)	2.601(4)
O(3)–Eu(1)–O(6)	93.87(14)	O(2)–Eu(1)–O(1)	69.50(11)
O(3)–Eu(1)–O(4)	71.04(11)	O(3)–Eu(1)–N(1)	100.59(12)
O(6)–Eu(1)–O(4)	77.08(15)	O(6)–Eu(1)–N(1)	145.19(13)
O(3)–Eu(1)–O(5)	147.45(12)	O(2)–Eu(1)–N(2)	75.86(13)
O(4)–Eu(1)–O(2)	130.60(13)	O(1)–Eu(1)–N(2)	81.27(12)
O(5)–Eu(1)–O(2)	128.52(13)	N(1)–Eu(1)–N(2)	64.98(11)

Fig. 1   Single-crystal X-ray structures of (a) **Eu1** and (b) **Eu2**. The displacement ellipsoids have been drawn with 50% probability (c) trigonal dodecahedral coordination polyhedron. Hydrogen atoms are omitted for clarity.
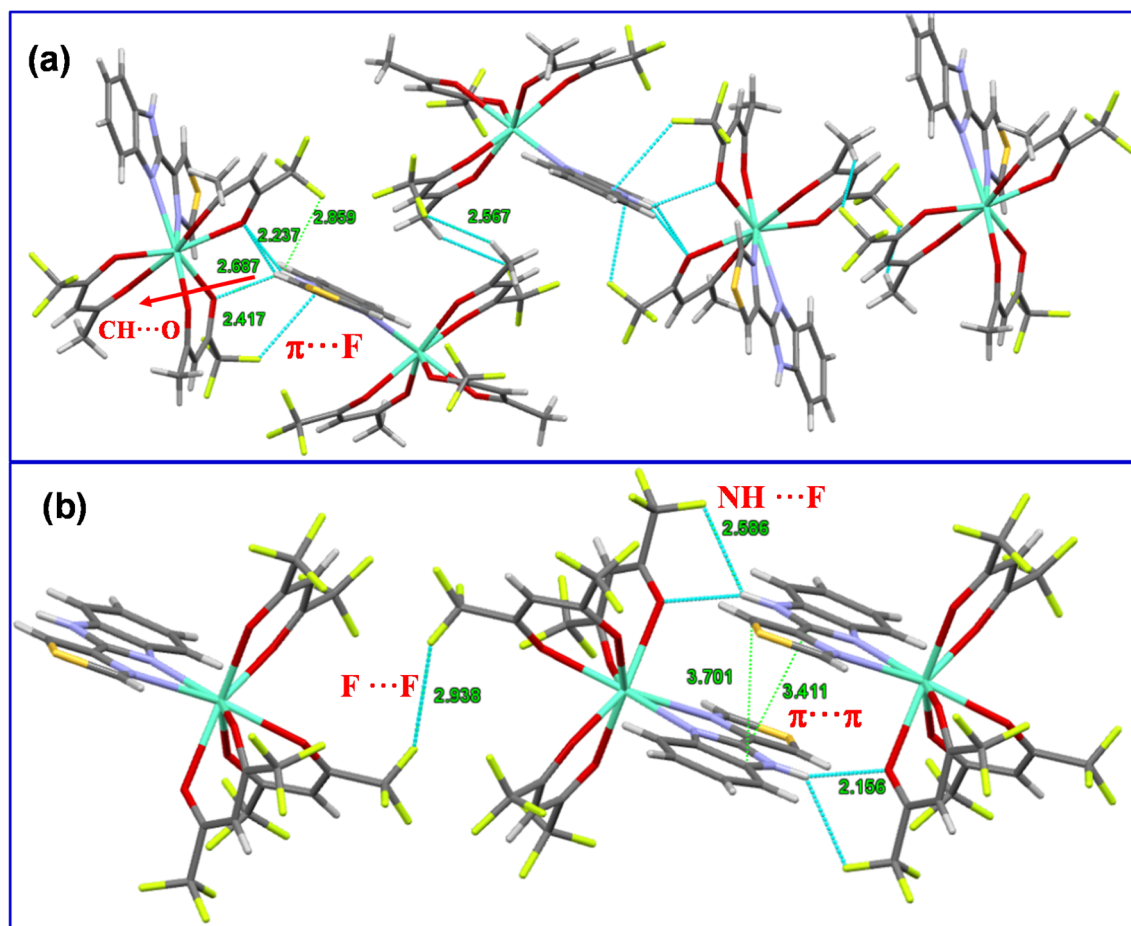
Fig. 2 Packing diagram of the complexes displaying different interactions (a) **Eu1** and (b) **Eu2**.

shown in Table S4, ESI.† Contrary to our previous work,[9a,b] the TZVPPD basis set (PBE1PBE/TZVPPD/MWB52) provided the best results for all the atoms in the complexes (Table S4, ESI†).

It is important to establish the solid-state packing in a given complex since it helps to understand the thermal and optical properties. The packing diagram of **Eu2** exhibits an extensive set of π···π stacking interactions of 3.411 Å and 3.781 Å between the aromatic rings of adjacent ligands to generate a one-dimensional (I-D) chain structure along the *a*-axis (Fig. 2b). Interestingly, **Eu1** does not show any sign of π···π interactions; however, a π···F (2.417 Å) interaction is observed between the aromatic ring of the TB-Im ligand and tfac ligand within the crystal lattice that generates a long chain of stacked molecules along the crystallographic *a*-axis (Fig. 2a). For **Eu1** there is an intermolecular N–H···O hydrogen bond involving the N–H unit of the TB-Im ligand (N(2)–H(2)···O(2^i), H(2)···O(2^i) 2.24 Å, N(2)···O(2^i) 3.028(5) Å, N(2)–H(2)···O(2^i) 153°; symmetry code (i) $\frac{1}{2} - x$, $-\frac{1}{2} + y$, $\frac{1}{2} - z$). There is also a relatively short C–H···F intermolecular interaction (C(11)–H(11b) ···F(6^{ii}), H(11b)···F(6^{ii}) 2.54 Å, C(11)···F(6^{ii}), 3.461(10) Å, C(11)–H(11b)···F(6^{ii}) 161°; symmetry code (ii) $\frac{1}{2} + x$, $3/2 - y$, $-\frac{1}{2} + z$). The N–H unit in **Eu2** also participates in a hydrogen bond
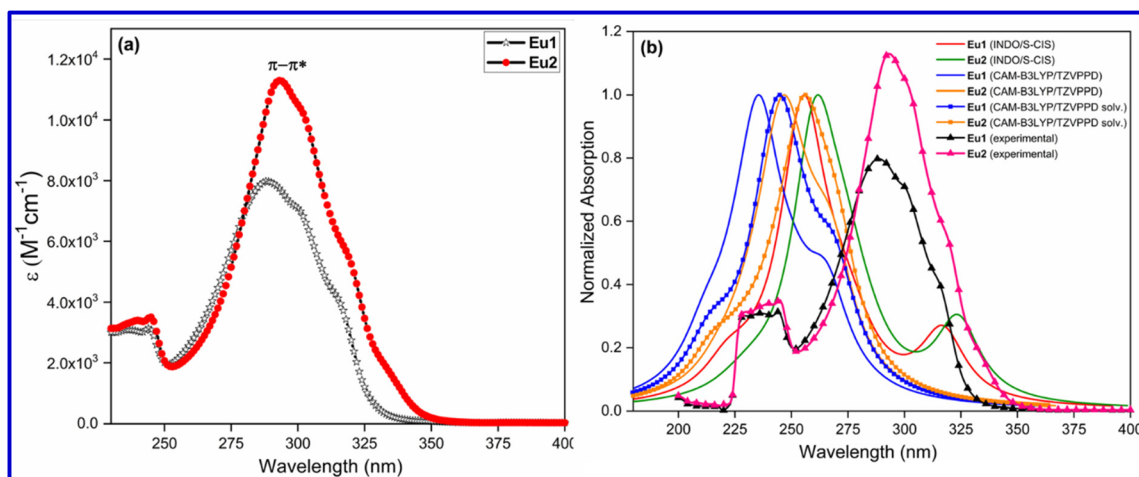
(N(3)–H(3)···O(1^{iii}), H(3)···O(1^{iii}) 2.16 Å, N(3)···O(1^{iii}) 2.915(6) Å, N(3)–H(3)···O(1iii) 147°; symmetry code (iii) $1 - x$, $1 - y$, $1 - z$), there is also a NH···F (2.586 Å) interaction with one of the hfac ligands, and F···F interactions (2.938 Å) between the molecules.

3.2. Photophysical studies

Optical absorption spectroscopy was used to evaluate the light absorbing capability of the complexes. The complexes displayed broad spectra in the region between 250 and 350 nm with λ_{abs}^{max} at 287 nm ($\varepsilon = 8041$ M^{-1} cm^{-1}) and 293 nm ($\varepsilon = 11\,375$ M^{-1} cm^{-1}) for **Eu1** and **Eu2**, respectively, attributed to a composite of π–π* transitions of both primary antenna and ancillary ligands (Fig. 3a). Moreover, the spectrum of **Eu2** displayed a minor (6 nm) but meaningful redshift in λ_{abs}^{max} compared to that of **Eu1**. This could be attributed to the greater number of fluorine (F) atoms on the ligands in **Eu2** which is favourable for inducing increased intramolecular charge transfer (ICT).[19]

To rationalize the experimental optical absorption spectroscopy results, we calculated the theoretical absorption spectra by the TD-DFT and INDO/S-CIS methods (Fig. 3b) employing the optimized geometry with the PBE1PBE/TZVPPD/MWB52 level of theory. As can be seen from Fig. 3b,

Fig. 3 (a) Optical absorption spectra of **Eu1** and **Eu2** in DCM solution (1×10^{-5} M). (b) Overlapped experimental and theoretical absorption spectra calculated by the TD-DFT (with and without the effect of solvent) and INDO/S-CIS methods for **Eu1** and **Eu2** using the geometry optimized at the PBE1PBE/TZVPPD/MWB52 level of theory.

the $\lambda_{\mathrm{max}}^{\mathrm{abs}}$ value is marginally under calculated which is similar to our recent study, where different TD-DFT methods (CAM-B3LYP, M06-2X, PBE1PBE and ωB97X-D3BJ) were used.[9b] However, the band shape and redshift (*ca.* 9 nm) of spectra obtained by the TD-DFT methods are in qualitative agreement with the experimental spectra of **Eu1** and **Eu2** suggesting that the TD-DFT approach could be an important tool to provide the most relevant electronic transitions to the most intense band.

The electronic transitions calculated at the CAM-B3LYP/TZVPPD/MWB52 level of theory, considering the effect of the DCM solvent, are presented in Table 2. It is possible to observe that the most important molecular orbitals (MOs) involved in the most intense band range from HOMO−4 to LUMO+4. The
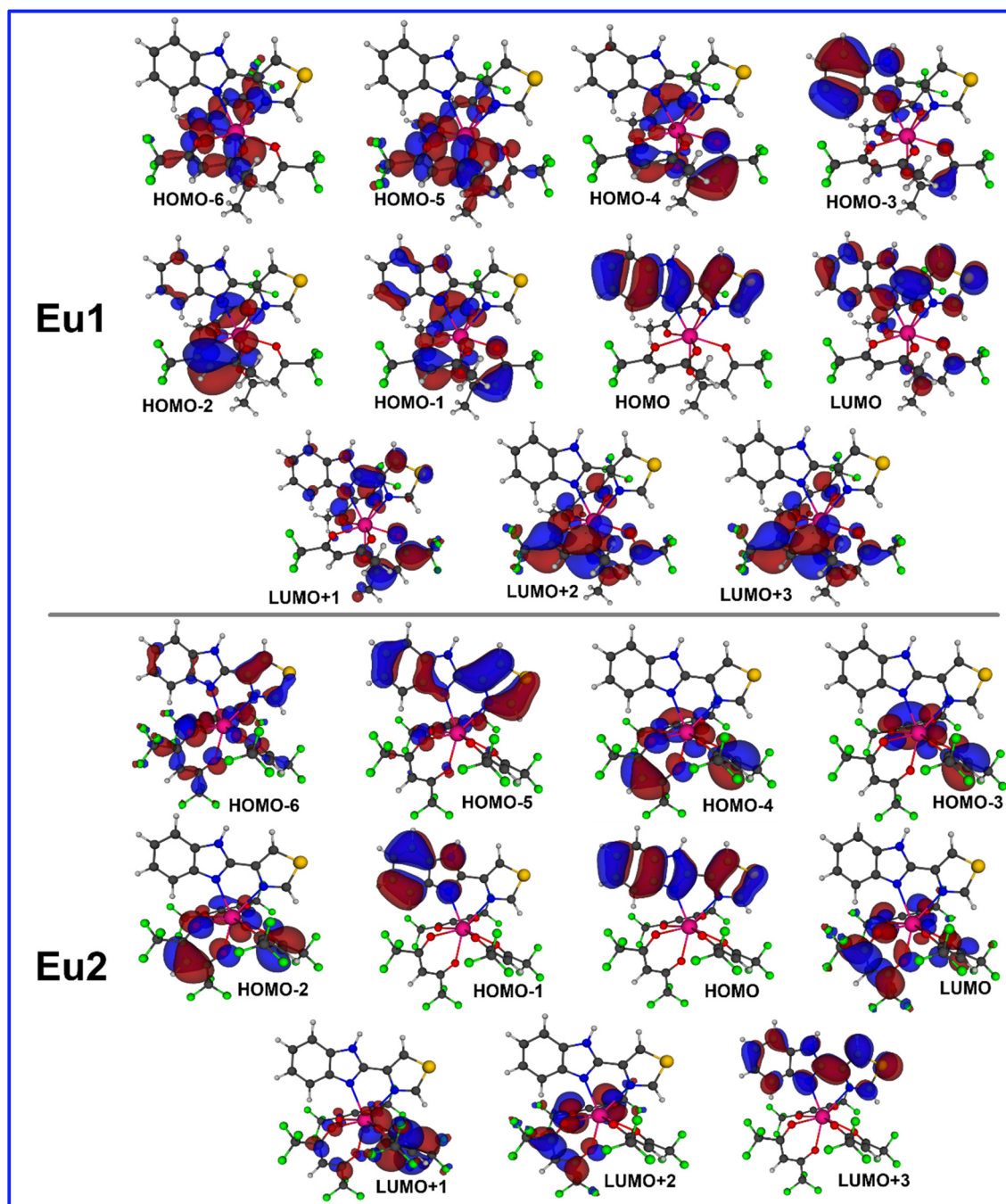
Table 2 Electronic transitions calculated at the CAM-B3LYP/TZVPPD/MWB52 level of theory for the most intense bands of **Eu1** and **Eu2** considering the effect of the DCM solvent

	λ, nm/oscillator strength	Major contribution	Total
Eu1	246.3/0.7912	**HOMO−1** → LUMO+3 (17.88%)	68.90%
		HOMO−4 → **LUMO+1** (13.62%)	
		HOMO−3 → LUMO (13.43%)	
		HOMO−2 → LUMO+2 (11.59%)	
		HOMO−1 → **LUMO+1** (6.31%)	
		HOMO−2 → LUMO (6.07%)	
	269.0/0.5553	**HOMO** → LUMO (60.81%)	83.78%
		HOMO → **LUMO+1** (17.46%)	
		HOMO → LUMO+4 (5.50%)	
Eu2	254.4/0.9220	**HOMO** → LUMO+1 (28.41%)	72.19%
		HOMO → LUMO (21.12%)	
		HOMO → LUMO+2 (10.90%)	
		HOMO−2 → LUMO (6.64%)	
		HOMO−4 → LUMO+1 (5.12%)	
	270.7/0.4056	**HOMO** → **LUMO+3** (60.77%)	76.92%
		HOMO−2 → LUMO (10.59%)	
		HOMO → LUMO+4 (5.55%)	

MOs centred on the ancillary ligand are highlighted in bold.

most intense bands of both complexes are due to electronic transitions involving MOs centred both in the primary β-diketonate and ancillary ligands (Fig. 4). The natural transition orbitals (NTOs) analysis performed at the same level of theory (Fig. S6, ESI†) further corroborated this observation. This analysis provides a simple representation of the transition density between the ground and the excited state[20] and reveals additionally that the longest wavelength band of **Eu1** is due to the electronic transitions involving MOs centred on the ancillary ligand. It is important to mention that the ligand containing a greater number of F-atoms provides a larger electron density resulting in a larger contribution to the band. Similar conclusions are obtained from the analysis of the TD-DFT results without considering the implicit effect of the DCM solvent (Table S5 and Fig. S7, ESI†).

Exciting the complexes at their $\lambda_{\mathrm{abs}}^{\mathrm{max}}$ exhibited five typical well-resolved emission transitions a–e (Table 3) in the region between 550–750 nm (Fig. 5) without any residual ligand fluorescence (RFL) between 380–500 nm (Fig. S8 and S9, ESI†) implying good energy transfer ET. Table 3 shows the barycentre of the emission transitions (a–e) and % contribution of the transition intensities relative to the magnetic dipole (MD) $^5D_0 \rightarrow {}^7F_1$. The intensity of the emission spectra follow a similar trend as the molar absorptivity values *i.e.*, **Eu2** > **Eu1**. The spectra of both complexes are dominated by the narrow (FWHM < 4 nm) electric dipole (ED) $^5D_0 \rightarrow {}^7F_2$ transition with a contribution greater than 78% of the total emission intensity. Moreover, the superiority of the ED transition over the MD transition indicates dynamic coupling (DC) as the dominant mechanism in the emission process.[21] From the emission spectra of the complexes, we further calculated the CIE coordinates of the emitted colour (Table 3). As can be seen from the inset of Fig. 5 (Fig. S10 and S11, ESI†) both the complexes displayed pure red emission with CIE coordinates very close to recommended CIE by NTSC (*x*, 0.67; *y*, 0.33) for red emission.

Fig. 4 Most relevant MOs calculated at the TD–DFT CAM-BLYP level of theory that explains the main electronic transitions. The implicit effect of the DCM solvent was considered in the calculation.

Apart from the steady-state emission studies, it is of importance to establish other potential experimental photophysical parameters to fully understand the emission phenomena in a given complex before their potential use in optoelectronic devices such as OLEDs can be established. In this regard, we first determined the excited lifetime (τ_{obs}) of the $^5D_0$ emitting state of **Eu1** and **Eu2** in solution. The τ_{obs} was calculated by the fitting of the PL decay curve (Fig. S12, ESI†) as shown in Fig. S13 and S14, ESI.† The PL decay profiles for both the com-
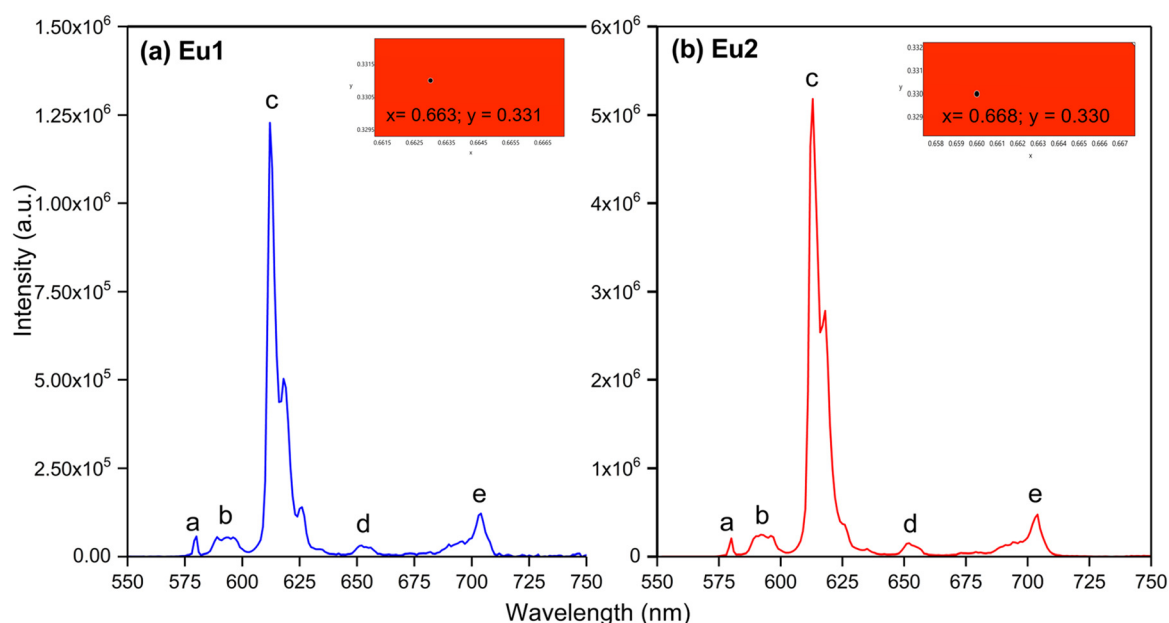
plexes reveal monoexponential behaviour and confirm the presence of single emitting species. This is supported by the crystal structure determinations of the complexes and further corroborates the steady-state emission spectra where a single well-resolved emission peak is observed for $^5D_0 \rightarrow {}^7F_0$. The τ_{obs} values in the microsecond timescale regime (**Eu1** = 885 ± 2.37 μs and **Eu2** = 977± 1.82 μs, Table 3) are well within the range of typical europium β-diketonate N^N complexes. The absolute PLQY (Q_{Eu}^L) of the complexes follows a similar trend

Table 3 Experimental and theoretical photophysical properties of **Eu1** and **Eu2** in DCM

Photophysical parameters	Eu1	Eu2
$^5D_0 \rightarrow {}^7F_0$ (a)	17 261.32 cm^{-1} (1.09%)	17 247.68 cm^{-1} (0.86%)
$^5D_0 \rightarrow {}^7F_1$ (b)	16 880.18 cm^{-1}	16 863.62 cm^{-1}
$^5D_0 \rightarrow {}^7F_2$ (c)	16 237.29 cm^{-1} (78.63%)	16 236.99 cm^{-1} (80.36%)
$^5D_0 \rightarrow {}^7F_3$ (d)	15 298.74 cm^{-1} (2.73%)	15 324.53 cm^{-1} [2.61%]
$^5D_0 \rightarrow {}^7F_4$ (e)	14 286.42 cm^{-1} (11.35%)	14 308.93 cm^{-1} (10.33%)
FWHM of $^5D_0 \rightarrow {}^7F_2$	3.76 nm	3.36 nm
Intensity ratio (R_{21})	12.88	14.02
CIE color coordinates	$x = 0.663$; $y = 0.331$	$x = 0.668$; $y = 0.330$
τ_{obs}	885 ± 2.37 μs ($\chi^2 = 1.002$)	977± 1.82 μs ($\chi^2 = 1.021$)
Ω_2 ($\times 10^{-20}$ cm^2)	22.66 × 10^{-20} cm^2 [22.61 × 10^{-20} cm^2]	24.57 × 10^{-20} cm^2 [24.57 × 10^{-20} cm^2]
Ω_4 ($\times 10^{-20}$ cm^2)	7.62 × 10^{-20} cm^2 [7.81 × 10^{-20} cm^2]	7.25 × 10^{-20} cm^2 [7.24 × 10^{-20} cm^2]
A_{Rad}	744.01 s^{-1} [721.90 s^{-1}]	786.18 s^{-1} [764.37 s^{-1}]
A_{NRad}	385.93 s^{-1} [408.04 s^{-1}]	236.52 s^{-1} [259.17 s^{-1}]
Q_{Eu}^{Eu}	65.84% [63.89%]	76.87% [74.68%]
Q_{Eu}^{L}	39.33% [38.32%]	47.00% [45.97%]
η_{Sen}	59.73% [59.98%]	61.14% [61.56%]

Values in the bracket are % contribution relative to MD transition; values in square parentheses are theoretically calculated; Ω_2 and Ω_4 were calculated by applying eqn (1) and (2); A_{Rad} and A_{NRad} were calculated by applying eqn (2) and (4); Q_{Eu}^{Eu} and η_{Sen} were calculated by applying eqn (6) and (7).

Fig. 5 PL spectra of (a) **Eu1** and (b) **Eu2** in DCM solution. Inset showing the magnified view of the CIE colour with their coordinates calculated from the emission spectra.

as noted for the steady-state emissions and the excited life-times. The complexes displayed fairly large values of Q_{Eu1}^{L} = 39.33% and Q_{Eu2}^{L} = 47.00% in solution. To understand it better, we have calculated A_{Rad} and A_{NRad} rates for the complexes by applying a set of eqn (2)–(4), which are presented in Table 3. It is clear from Table 3 that the large Q_{Eu2}^{L} value of **Eu2** compared to **Eu1** is due to the lower A_{NRad} = 236.52 s^{-1} of **Eu2**, which is further reflected in its Q_{Eu}^{Eu} = 76.87% leading to sensitization efficiency of η_{Sen} = 61.14%. Finally, J–O intensity parameter (Ω_2 and Ω_4) was calculated (Table 3). In each case Ω_2

displayed a large value implying that the symmetry around the Eu(III) is distorted which indeed is the case as determined by the single-crystal structure determinations (distorted triangular dodecahedron). As expected, Ω_2 value of **Eu2** (24.57 × 10^{-20} cm^2) is larger than that of **Eu1** (22.66 × 10^{-20} cm^2), which is due to more distorted coordination geometry at the Eu(III) centre; in **Eu2** (CShM = 0.695) compared to **Eu1** (CShM = 0.629). The Ω_4 parameter is less sensitive to the coordination sphere; however, it is related to long-range effects (hydrogen bonding and π–π stacking).[21] The significantly large value of

the $\Omega_4 = 7.62 \times 10^{-20}$ cm^2 and 7.25×10^{-20} cm^2 for **Eu1** and **Eu2**, respectively, points to the presence of these effects. This is further supported by the single crystal X-ray structure where these long-range effects are encountered. The theoretically calculated Ω_2 and Ω_4 (Table 3) using the QDC model[22] (Table S6, ESI†) and A_{Rad} compare well with the experimental data (Table 3). Moreover, we further calculated the contribution of the forced electric dipole intensity parameters Ω_λ^{FED}. The low values of Ω_λ^{FED} (Table S6, ESI†) attest that the emission for the present complexes is dominated by the dynamic coupling (DC) mechanism, a commonly observed phenomenon in these types of complexes. Furthermore, a low value of Ω_λ^{FED} indicates that Ω_λ is strongly dependent on the polarizabilites of the ligand atoms of the complexes. It is worth mentioning that Ω_λ^{FED} plays an important role in estimating the ET rates from the direct coulombic interaction (CI) mechanism which is operative when the J quantum number of the states of the Eu (III) ion involved in the electronic excitations satisfy the $|\Delta J| =$ 2, 4, and 6 selection rule.

3.3. Intermolecular energy transfer (IET)

TD-DFT calculations were also performed to evaluate the impact of the geometry on the lowest energy singlet (S_1) and triplet states (T_1). The TD-DFT CAM-B3LYP/TZVP/MWB52 approach was applied considering all the optimized geometries by the different DFT methods (Table S7, ESI†). It is important to emphasize that R_L parameter and energy of S_1 and T_1 varied modestly which could be attributed to the similar RMSD values in each structure (Table S4, ESI†). Moreover, a careful analysis of Table S6, ESI,† further revealed that the effect of solvent on the T_1 of **Eu2** is more prominent than that on **Eu1**. The solvent caused an average stabilization of 285 cm^{-1} in the T_1 state of **Eu2** while this is only 25 cm^{-1} for **Eu1**. An explanation for this is that the electron density due to the various peripheral F atoms of hfac in **Eu2** interacts more strongly with the electric field produced by the solvent compared to tfac of **Eu1**. Using the default setting of LUMPAC[23] for INDO/S-CIS model, we found a much lower value for T_1 for both the complexes (14 550.3 and 14 424.1 cm^{-1} for **Eu1** and **Eu2**, respectively, Table S7, ESI†) which is in contrast to our recent work.[9a,c] The analysis of the electronic transitions involved in T_1 calculated by the INDO/S-CIS model showed that the most important MOs are situated on the TB-Im ligand. To confirm this behaviour, we further replaced the ancillary ligand by two water molecules and found the T_1 was around 20 000 cm^{-1} thus confirming that the lowering is due to the TB-Im ligand.

To propose the ET mechanism of the complexes, the results obtained using the TD-DFT CAM-B3LYP/TZVPPD/ MWB52 method (DCM solvent) with the geometry optimized at the PBE1PBE/TZVPPD/MWB52 level of theory were utilized. The ligand–metal ET rate for a given pathway depends on the energy and distance R_L of the excited states involved in the ET process (see eqn (S2) and (S3), ESI†). The energy of the lowest S_1 and T_1 states and their corresponding R_L value states are shown in Table 5. An analysis of the electronic transitions for S_1 and T_1 (Table 5) in conjunction with the MOs (Fig. 4)

suggests that S_1 and T_1 involved MOs centred on the β-diketonate and ancillary ligands. In case of **Eu2**, 93.4% of the electronic transitions that compose T_1 strongly depend on MOs centred only on the hfac ligands without any role of the TB-Im ligand. The analysis of MOs showed additionally that the lowest three triplet states of **Eu2** had almost similar energies ($T_1 = 22\,252.4$ cm^{-1}, $T_2 = 22\,385.9$ cm^{-1} and 22 622.0 cm^{-1}) and involved only MOs centred on the different β-diketones ligands. A slightly different situation was observed for the degenerate T_1 (24 326.3 cm^{-1}), T_2 (24 379.8 cm^{-1}) and T_3 (22 622.0 cm^{-1}) states of **Eu1**, since these states had contribution from TB-Im mainly through HOMO−3, HOMO−1, LUMO, and LUMO. The T_4 state (27 129.5 cm^{-1}) of **Eu2** is composed of MOs centred mainly on the TB-Im. The contribution of MOs centred on the TB-Im explains why the energy of T_1 for **Eu1** is higher than the corresponding state of **Eu2**.

The calculated ET rates for the complexes employing Malta's model[24] for different excited levels of Eu(III) and the excited states of the ligands are shown in Table 4 and Table S8, ESI.† ET channels that are governed by the CI and Ex. mechanisms are distinguished in Table S8† and the back ET rate (W_{BET}) was estimated by using the sum where both mechanisms were operative. The largest value of ET rate (W_{ET}) observed for the S_1 state of **Eu1** is of the order of 10^5 s^{-1} and is related to the $^7F_1 \to {}^5G_{2,3}$ acceptor levels of Eu(III). Because of the resonance condition involving S_1 of **Eu2** and the $^5D_4$, $^5D_3$ and $^5G_3$ states, rates of this order were observed for $^7F_0 \to {}^5D_4$, $^7F_1 \to {}^5D_3$ and $^7F_1 \to {}^5G_3$ acceptors, where all these rates are governed by the CI mechanism. A rate of the order of 10^6 was observed for the $^7F_1 \to {}^5G_2$ acceptor for **Eu2** and is dominated by the Ex. mechanism. Since S_1 of both complexes were overestimated, W_{BET} involving all the excited states considered for Eu (III) are practically negligible. When the ET pathways from T_1 is analysed, it is noted that the $^7F_1 \to {}^5D_0$ state has W_{ET} value of 10^8 and 10^9 s^{-1} for **Eu1** and **Eu2**, respectively, revealing the importance of this channel in sensitizing the PL of the complexes. Table S8† shows large values of W_{BET} for some pathways involving T_1. In these cases, since the states of the Eu(III) ion are significantly above T_1, the energy returns to T_1 which can then be transferred to more resonant states of Eu(III) such as the $^5D_0$ and $^5D_1$ states. Moreover, ET from T_4 state in **Eu2** provides a significant value of rate (10^7 s^{-1}) for the pathways related to $^7F_0 \to {}^5D_1$ (3.24 × 10^7 s^{-1}), $^7F_1 \to {}^5D_0$ (2.79 × 10^7 s^{-1}) and $^7F_1 \to {}^5D_2$ (1.54 × 10^7 s^{-1}). The R_L value for T_4 is sufficiently small (3.1828 Å) to favour the ligand-Eu(III) ET. A rate of 10^8 s^{-1} is noted for the $T_4 \to {}^7G_2$ channel; however, a considerable W_{BET} is obtained due to the good resonance condition between T_4 and $^5G_2$ (9.80 × 10^6 s^{-1}; Table S8, ESI†).

The most important energy migration channels for the sensitized PL of the complexes are depicted as the Jablonski diagram (Fig. 6). Since the experimental η_{Sen} for both the complex is ≈60%, a plausible explanation for these experimental observations could be due to the presence of pathways that eventually depopulates to T_1. To reproduce the experimental results some rates involving ligand states were adjusted as already applied in previous work.[9b] As can be seen in Fig. 6,

Table 4 Energy of the S and T excited states, distance from energy donor to acceptor centre (R_L), and electronic transitions for the corresponding excited states of the complexes calculated with the TD-DFT CAM-B3LYP/TZVPPD/MWB52 approach considering the effect of DCM

Compound	State	Energy/cm^{-1}	R_L/Å	Major contribution	Total
Eu1	S$_1$	35 475.1	3.4485	HOMO−6 → LUMO+3 (32.83%)	89.18%
				HOMO−6 → **LUMO+1** (14.25%)	
				HOMO−6 → LUMO+2 (9.80%)	
				HOMO−5 → LUMO+3 (9.64%)	
				HOMO−6 → **LUMO** (9.21%)	
				HOMO−5 → LUMO+2 (7.15%)	
				HOMO−5 → **LUMO+1** (6.29%)	
	T$_1$	24 326.3	3.6026	**HOMO−1 → LUMO+1** (27.66%)	84.14%
				HOMO−4 → LUMO+3 (17.40%)	
				HOMO−4 → LUMO+2 (11.48%)	
				HOMO−1 → LUMO (9.89%)	
				HOMO−4 → **LUMO+1** (9.52%)	
				HOMO−3 → LUMO+1 (8.19%)	
Eu2	S$_1$	34 505.5	3.2805	**HOMO−6** → LUMO+2 (26.04%)	88.04%
				HOMO−6 → LUMO (17.21%)	
				HOMO−7 → LUMO+2 (15.53%)	
				HOMO−5 → LUMO+2 (9.19%)	
				HOMO−8 → LUMO+2 (8.07%)	
				HOMO−7 → LUMO (6.30%)	
				HOMO−5 → LUMO (5.70%)	
	T$_1$	22 252.4	3.2957	HOMO−2 → LUMO (38.87%)	93.40%
				HOMO−4 → LUMO (19.17%)	
				HOMO−2 → LUMO+2 (16.89%)	
				HOMO−4 → LUMO+2 (12.68%)	
				HOMO−4 → LUMO+1 (5.79%)	
	T$_4$	27 129.5	3.1828	**HOMO → LUMO+3** (78.57%)	85.22%
				HOMO−5 → LUMO+3 (6.66%)	

MOs highlighted in bold are those centred in the ancillary ligand.

Fig. 6 Schematic energy-level diagram for (a) **Eu1** and (b) **Eu2**, showing the states considered in the modelling of the ET of both complexes.

decay rates for **Eu1** involving the S$_1$ → T$_1$ and T$_1$ → S$_1$ pathways of the order of 10^6 and 10^7 s^{-1}, respectively, provided a theoretical η_{Sen} = 60.0%, which agrees with the experimental η_{Sen} = 59.73%. The energy-level diagram for **Eu2** shows that rates of the order 10^5, 10^9 and 10^9 s^{-1} for S$_1$ → T$_4$, T$_4$ → T$_1$ and T$_1$ → S$_0$ provided a theoretical η_{Sen} of 61.6%. It is important to mention that the other experimental photophysical parameters were also reproduced well for both complexes.

3.4. Electroluminescence and electrophysical properties of Eu1 and Eu2 based OLEDs

The thermal stability of **Eu1** and **Eu2** is of critical importance since inferior thermal stability of the complex tends to reduce device stability, especially at the peak of its operation. This is due to the Joule heating when current flows through the organic layers.[21] In view of this, the thermal stability of **Eu1**
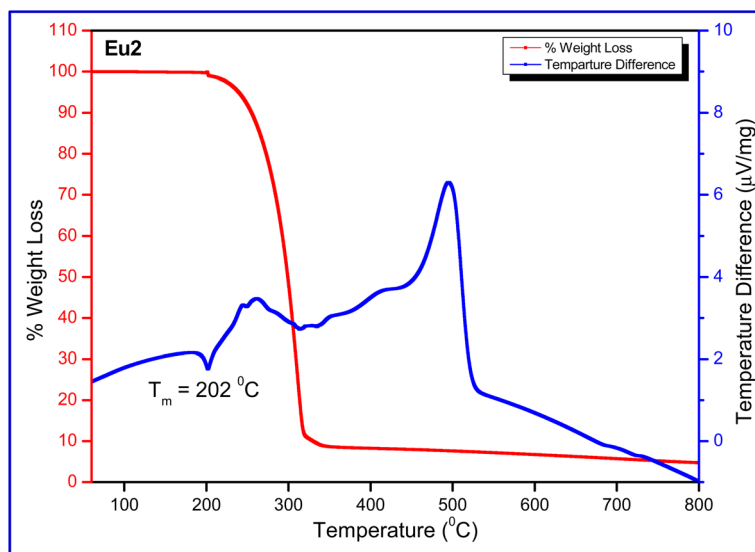
Fig. 7 TGA and DTA profile of **Eu2** under N$_2$ atmosphere.

and **Eu2** in the temperature range between 50–800 °C under a dinitrogen (N$_2$) atmosphere was determined. The thermogram of the complexes (Fig. 7 and Fig. S15, ESI†) does not exhibit any weight loss in the 50–150 °C region, implying that complexes have no lattice held/coordinated solvent/water molecules as is evident from the FT-IR and crystallographic studies. The DTA of the complexes displayed an endothermic peak at 228.9 and 202 °C for **Eu1** and **Eu2**, respectively, representing the melting temperature (T_m). It is noteworthy that T_m of **Eu1** is higher than **Eu2** which possibly could be attributed to π⋯F (2.417 Å) interactions within the crystal lattice. The decomposition temperature (T_d) with 5% weight loss of the complexes is 241 °C for **Eu1** and 239 °C for **Eu2**, respectively. The high thermal stability of the complexes implies that they can easily be employed to fabricate OLEDs by the vacuum thermal evaporation method.

Realizing the good PL and thermal properties of **Eu1** and **Eu2** and to fully establish their potential as an active component in OLEDs, we finally fabricated OLEDs by the vacuum thermal evaporation method and evaluated their EL and elec-

trophysical properties. To investigate EL performances of the complexes, multilayers OLEDs were fabricated (please see ESI† for device details). The doping concentrations of the active component (**Eu1** and **Eu2**) were varied. Interestingly, as the doping concentration increased the temperature of evaporation (T_{evp}) increased simultaneously gradually [145–154 °C for **Eu1** and 139–149 °C for **Eu2**]. However, it remained very low compared to T_m and T_d [T_m = (228.9 °C)$_{Eu-1}$ and (202 °C)$_{Eu2}$ and T_d = (241 °C)$_{Eu-1}$ and (239 °C)$_{Eu2}$] during the fabrication processes of the devices and implies that no decomposition and melting of the complexes occurred, thus EL arising in the OLEDs are due to complexes. The EL performance data obtained such as brightness (B), current efficiency (η_c), power efficiency (η_p), external quantum efficiency (EQE) and CIE colour coordinates for single-EML as well as double-EML OLEDs of **Eu1** and **Eu2** at J = 10 mA cm^{-2} are summarized in Table 5 and Table S9, ESI.†

As can be seen the EL spectra of the single- and double-EML devices of both **Eu1** and **Eu2** (Fig. 8) displayed emission

Table 5 Key electroluminescent properties of the single-EML devices of **Eu1** and **Eu2** operating at J = 10 mA cm^{-2}

Doping concentration (device)	$V_{turn-on}$ (V)	B^a (cd m^{-2})	$\eta_c{}^b$ (cd A^{-1})	$\eta_p{}^c$ (lm W^{-1})	EQE	CIE$_{x,y}{}^d$
Eu1						
2 wt% (Device 1)	5.0	32.56	0.068	0.034	0.044%	(0.284, 0.264)
3 wt% (Device 2)	4.6	55.11	0.079	0.046	0.049%	(0.354, 0.288)
4 wt% (Device 3)	4.6	100.5	0.109	0.055	0.068%	(0.329, 0.285)
5 wt% (Device 4)	4.6	29.47	0.049	0.027	0.035%	(0.294, 0.243)
6 wt% (Device 5)	5.4	21.52	0.048	0.025	0.030%	(0.285, 0.282)
Eu2						
2 wt% (Device 1)	3.5	710.4	0.441	0.396	0.304%	(0.283, 0.199)
3 wt% (Device 2)	3.5	736.1	0.524	0.461	0.327%	(0.305, 0.220)
4 wt% (Device 3)	3.9	364.1	0.276	0.223	0.186%	(0.333, 0.228)
6 wt% (Device 4)	4.1	238.8	0.229	0.176	0.150%	(0.386, 0.259)
8 wt% (Device 5)	4.1	186.2	0.205	0.157	0.135%	(0.386, 0.256)

^{a} The data for maximum brightness (B). ^{b} Maximum current efficiency (η_c). ^{c} Maximum current efficiency (η_p). ^{d} CIE at J = 10 mA cm^{-2}.
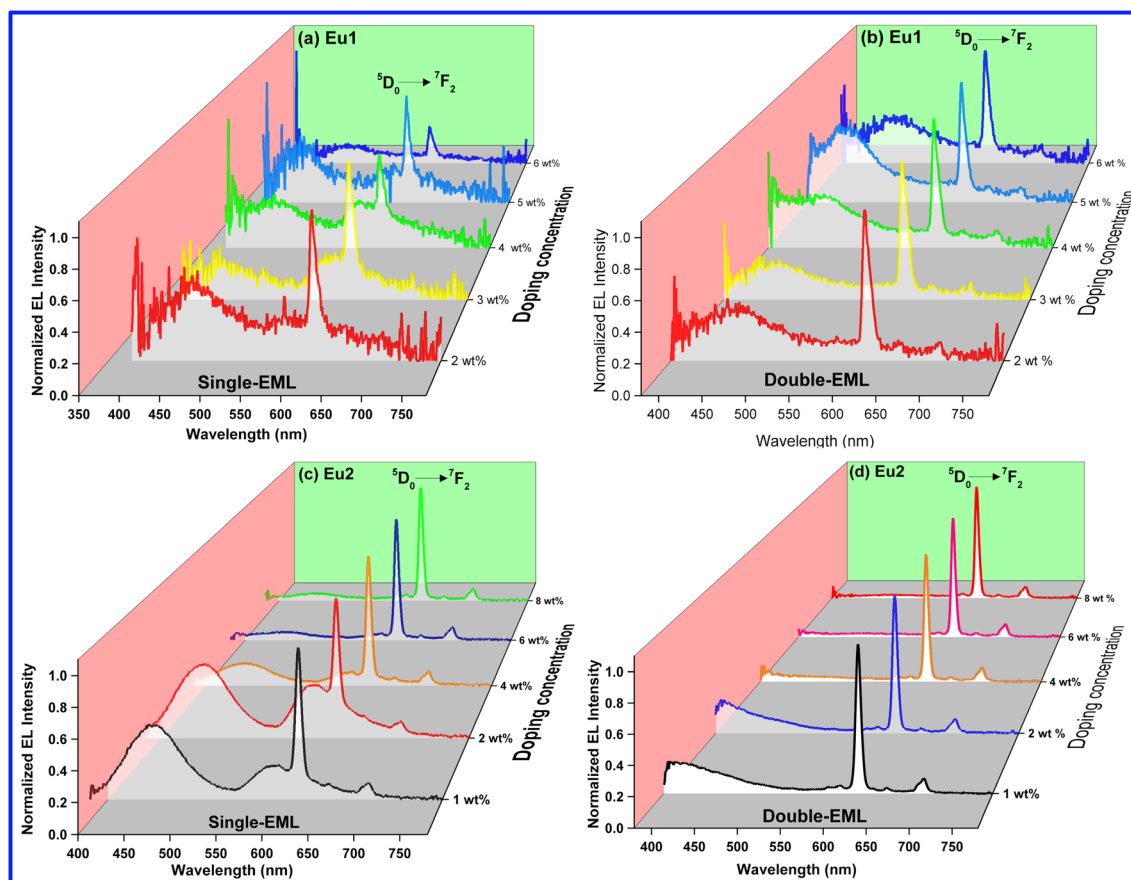
Fig. 8 Normalized EL spectra of single- and double-EML devices of **Eu1** and **Eu2** at different doping concentrations operating at $J = 10$ mA cm^{-2}.
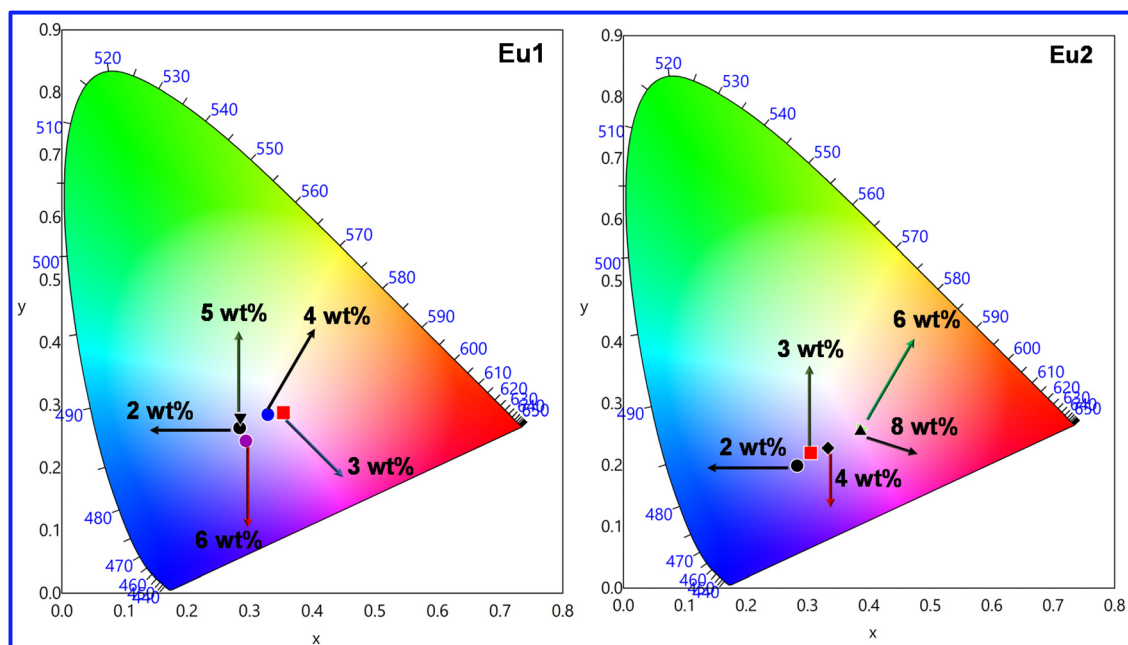

Fig. 9 CIE 1931 chromaticity diagrams of single-EML **Eu1** and **Eu2** based devices at different doping concentrations operating at $J = 10$ mA cm^{-2}.
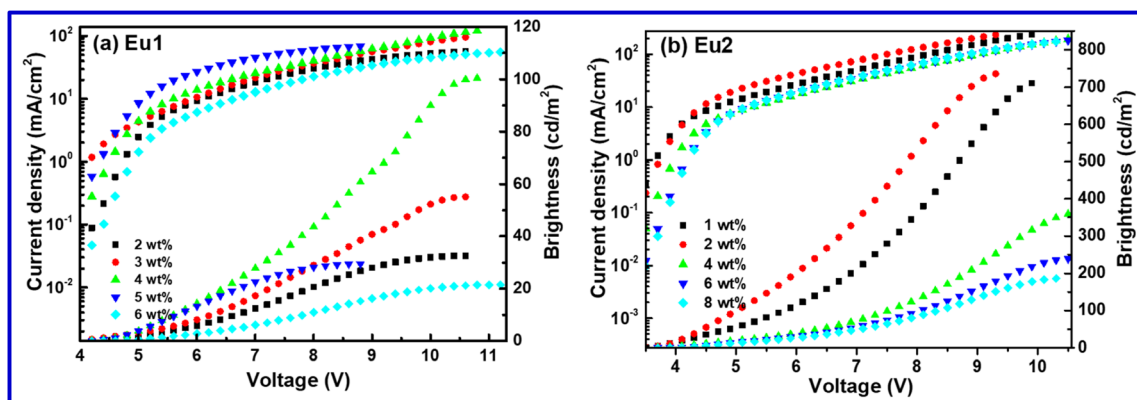
Table 6 A comparative electroluminescent characteristic of single component W-OLEDs

Complex	B^a (cd m^{-2})	$V_{\text{turn-on}}$ (V)	η_p (lm W^{-1})	CIE	Ref.
Eu1	55.11	4.6	0.034	0.354, 0.288	This work
Eu2	736.1	3.5	0.461	0.305, 0.220	This work
[Eu(TCPD)$_3$Phen]	229	20.5	0.2 (10.5 V)	0.333; 0.348	26a
[Eu(tta)$_3$L]	945.1	16	—	0.337; 0.362	27
[Eu$_2$(tta)$_6$]bpm	19.7	7.6	—	0.350; 0.330	26b

Where TCPD = 1-[3,4,5-tris[4-(9H-carbazol-9-yl)butoxy]-phenyl]-3-phenylpropane-1,3-dione; Phen = 1,10-phenanthroline; tta = thenoyltrifluoroacetonate; L = 2-(3,5-dimethyl-2H-pyrrol-2-yl)-4-(3,5-dimethyl-3H-pyrrol-2-yl)-6-(4-(pentan-3-yl)phenyl)-1,3,5-triazine; bpm = 2,2′-bipyrimidine. ^{a} The data for maximum brightness (B) and be placed after the definitions of the ligands on a new line.

Fig. 10 Current density (J)–voltage (V)–brightness (B) curve of the single component OLEDs of (a) **Eu1** and (b) **Eu2**.

transitions originating from the Eu(III) ion implying that both carrier-trapping and Förster ET are taking part in the device luminescent processes.[9b–d,21] Moreover, EL spectra of **Eu1** and single-EML **Eu2** devices exhibited broad host emission in the region between 380–550 nm similar to the PL spectra of the doped films except the change in the intensity (Fig. S16–S19, ESI†). The presence of broad emission suggests that ET from host to Eu(III) ion is small. Moreover, the intensity of host emission for **Eu1** based devices increased with the doping concentration except for the 6 wt% device, impling poor carrier-trapping on the **Eu1** molecules and incomplete ET from the host to Eu(III) molecules. However, this trend is reversed for **Eu2** based devices implying enhanced carrier-trapping and improved ET from host to **Eu2** molecules.

The host emission in the region between 400–500 nm coupled (Fig. S20, ESI†) with the typical red emission of Eu(III) ion at 600–620 nm due to the electric dipole $^5D_0 \rightarrow {}^7F_2$ transition prove beneficial in obtaining colour tunable OLEDs (Fig. 9, Fig. S21 and S22, ESI†). At the 4 wt% (**Device 3**) doping concentration, the emission of devices based on **Eu1** and **Eu2** fall in the white light emission region with CIE colour coordinates of (0.329, 0.285)$_{\text{Eu1}}$ and (0.333, 0.228)$_{\text{Eu2}}$ (Table 6), respectively. Furthermore, we have calculated the colour correlated temperature (CCT) of the emitted light that measures the coolness and warmness of the light by the McCamy method.[25] The CCT values of **Device 3** for **Eu1** (5719 K) and **Eu2** (5356 K) fall in the cool white light category and thus could be a poten-

tial candidate for lighting that will represent the real colour of the objects *i.e.*, kitchen, garage, workshop, product displays, industrial applications, *etc*.

The current density (J)–voltage (V)–brightness (B) curves are shown in Fig. 10 and Fig. S23 & S24, ESI† for **Eu1** and **Eu2**, respectively. The detailed EL performances such as B, η_c, η_p and EQE of single- as well as double-EML devices based on **Eu1** and **Eu2** are summarized in Table 5 & Table S9, ESI.† The white-OLED of **Eu1** displayed B = 100.5 cd m^{-2}, η_c = 0.109 cd A^{-1}, η_p = 0.055 lm W^{-1}, EQE = 0.068% with the turn-on voltage = 4.6 V, while **Eu2** based W-OLED exhibited improved EL performance (B = 364.1 cd m^{-2}, η_c = 0.276 cd A^{-1}, η_p = 0.223 lm W^{-1}, EQE = 0.186% with the very low turn-on voltage = 3.9 V). It is important to mention that the electroluminescent properties of the present single component white-OLEDs are higher than the reported ternary europium complexes.[26]

4. Conclusion

Two new OEuCs were succesfully synthesized and structurally charcaterized. Analysis of the crystallographically determined molecular structures through the CShMs analysis revealed that the geometry around the Eu(III) centre is distorted triangular dodecahedral, with approximate D_{2d} symmetry' in both structures. The complexes displayed fairly strong light absorbing capability and the most intense

absorption transitions are a composite of MOs centred both on the primary β-diketonate and ancillary ligands. NTOs analysis also revealed that ligand with greater number of Fatoms provides a larger electron density and thus results in a larger contribution to the most intense transition. Exciting the complexes at their λ_{abs}^{max} exhibited typical well-resolved red emission with reasonable Q_{Eu}^{L} value. A close scrutiny of the TD-DFT results suggest that electronic transitions that compose T_1 in **Eu2** (93.4%) exclusively rely on the MOs of hfac while for **Eu1** both tfac and Tb-Im MOs are involved resulting in higher T_1 state in **Eu1** compared to **Eu2**. The $^7F_1 \rightarrow {}^5D_0$ state have large W_{ET} values of 10^8 and 10^9 s^{-1} for **Eu1** and **Eu2**, respectively, emphasising the significance of this channel in sensitizing the PL of the complexes. Finally, the complexes were successfully employed as EML to fabricate OLEDs. The emission of **Device 3** of **Eu1** and **Eu2** falls in the white light emission region with superior EL performance to the few reported single component white-OLEDs of ternary europium complexes. Furthermore, calculated CCT values fall in the cool white light category and points to its potential for lighting that will represent the real colour of the objects *i.e.*, kitchen, garage, workshop, product displays, industrial applications, *etc*.

Conflicts of interest

The authors declare no conflicts of interest.

Acknowledgements

References

1 (*a*) R. Ilmi, S. Kansız, N. K. Al-Rasbi, N. Dege, P. R. Raithby and M. S. Khan, *New J. Chem.*, 2020, **44**, 5673–5683; (*b*) R. Ilmi, M. S. Khan, W. Sun, L. Zhou, W.-Y. Wong and P. R. Raithby, *J. Mater. Chem. C*, 2019, **7**, 13966–13975; (*c*) Y. He, L. Liu, G. Fu, W. Li, X. Lü, H. He and W.-Y. Wong, *J. Mater. Chem. C*, 2019, **7**, 4800–4807; (*d*) R. Ilmi, M. S. Khan, Z. Li, L. Zhou, W.-Y. Wong, F. Marken and P. R. Raithby, *Inorg. Chem.*, 2019, **58**, 8316–8331; (*e*) R. Ilmi, E. Tseriotou, P. Stylianou, Y. A. Christou, I. Ttofi, N. Dietis, C. Pitris, A. D. Odysseos and S. N. Georgiades, *Mol. Pharm.*, 2019, **16**, 4260–4273.

2 M. Pan, W.-M. Liao, S.-Y. Yin, S.-S. Sun and C.-Y. Su, *Chem. Rev.*, 2018, **118**, 8889–8935.

3 (*a*) Y. Kitagawa, M. Tsurui and Y. Hasegawa, *RSC Adv.*, 2022, **12**, 810–821; (*b*) A. N. Al-Khalili, I. J. Al-Busaidi, R. Ilmi, M. Al-Mandhary, M. S. Khan and N. K. Al-Rasbi, *Inorg. Chim. Acta*, 2020, **501**, 119226.

4 K. Yanagisawa, Y. Kitagawa, T. Nakanishi, T. Seki, K. Fushimi, H. Ito and Y. Hasegawa, *Chem. – Eur. J.*, 2018, **24**, 1956–1961.

5 M. Rajendran, R. Devi, S. Mund, K. Singh and S. Vaidyanathan, *J. Mater. Chem. C*, 2021, **9**, 15034–15046.

6 (*a*) S. Sato and M. Wada, *Bull. Chem. Soc. Jpn.*, 1970, **43**, 1955–1962; (*b*) M. Latva, H. Takalo, V. M. Mukkala, C. Matachescu, J. C. RodriguezUbis and J. Kankare, *J. Lumin.*, 1997, **75**, 149–169.

7 (*a*) S. I. Weissman, *J. Chem. Phys.*, 1942, **10**, 214–217; (*b*) N. Sabbatini, M. Guardigli and I. Manet, in *Handbook on the Physics and Chemistry of Rare Earths*, ed. K. A. Gschneidner Jr. and E. LeRoy, Elsevier, 1996, vol. 23, pp. 69–119; (*c*) R. Ilmi, N. Hasan, J. Liu, D. Mara, R. Van Deun and K. Iftikhar, *J. Photochem. Photobiol., A*, 2017, **347**, 116–129.

8 (*a*) R. Ilmi, A. Haque, I. J. Al-Busaidi, N. K. Al Rasbi and M. S. Khan, *Dyes Pigm.*, 2019, **162**, 59–66; (*b*) R. Ilmi, S. Anjum, A. Haque and M. S. Khan, *J. Photochem. Photobiol., A*, 2019, **383**, 111968.

9 (*a*) I. J. Al-Busaidi, R. Ilmi, D. Zhang, J. D. L. Dutra, W. F. Oliveira, N. K. Al Rasbi, L. Zhou, W.-Y. Wong, P. R. Raithby and M. S. Khan, *Dyes Pigm.*, 2022, **197**, 109879; (*b*) R. Ilmi, D. Zhang, J. D. L. Dutra, N. Dege, L. Zhou, W.-Y. Wong, P. R. Raithby and M. S. Khan, *Org. Electron.*, 2021, **96**, 106216; (*c*) M. S. Khan, R. Ilmi, W. Sun, J. D. L. Dutra, W. F. Oliveira, L. Zhou, W.-Y. Wong and P. R. Raithby, *J. Mater. Chem. C*, 2020, **8**, 5600–5612; (*d*) R. Ilmi, W. Sun, J. D. L. Dutra, N. K. Al-Rasbi, L. Zhou, P.-C. Qian, W.-Y. Wong, P. R. Raithby and M. S. Khan, *J. Mater. Chem. C*, 2020, **8**, 9816–9827.

10 G. M. Farinola and R. Ragni, *Chem. Soc. Rev.*, 2011, **40**, 3467–3482.

11 T. N. Singh-Rachford and F. N. Castellano, *Coord. Chem. Rev.*, 2010, **254**, 2560–2573.

12 R. Ilmi, A. Haque and M. S. Khan, *J. Photochem. Photobiol., A*, 2019, **370**, 135–144.

13 K. Yanagisawa, T. Nakanishi, Y. Kitagawa, T. Seki, T. Akama, M. Kobayashi, T. Taketsugu, H. Ito, K. Fushimi and Y. Hasegawa, *Eur. J. Inorg. Chem.*, 2015, **2015**, 4769–4774.

14 L. Farrugia, *J. Appl. Crystallogr.*, 1999, **32**, 837–838.

15 (*a*) G. Sheldrick, *SADABS, Program for Empirical Absorption Correction of Area Detector Data*, University of Göttingen, Göttingen, Germany, 1996; (*b*) G. Sheldrick, *Acta Crystallogr., Sect. A: Found. Adv.*, 2015, **71**, 3–8.

16 C. F. Macrae, P. R. Edgington, P. McCabe, E. Pidcock, G. P. Shields, R. Taylor, M. Towler and J. van de Streek, *J. Appl. Crystallogr.*, 2006, **39**, 453–457.

17 R. Ilmi, S. Kansız, N. Dege and M. S. Khan, *J. Photochem. Photobiol., A*, 2019, **377**, 268–281.

18 (*a*) M. Pinsky and D. Avnir, *Inorg. Chem.*, 1998, **37**, 5575–5582; (*b*) D. Casanova, M. Llunell, P. Alemany and S. Alvarez, *Chem. – Eur. J.*, 2005, **11**, 1479–1494.

19 R. Ilmi, H. Al-Sharji and M. S. Khan, *Top. Curr. Chem.*, 2022, **380**, 18.

20 R. L. Martin, *J. Chem. Phys.*, 2003, **118**, 4775–4777.

21 R. Ilmi, D. Zhang, L. Tensi, H. Al-Sharji, N. K. Al Rasbi, A. Macchioni, L. Zhou, W.-Y. Wong, P. R. Raithby and M. S. Khan, *Dyes Pigm.*, 2022, **203**, 110300.

22 J. D. L. Dutra, N. B. D. Lima, R. O. Freire and A. M. Simas, *Sci. Rep.*, 2015, **5**, 13695.

23 J. D. Dutra, T. D. Bispo and R. O. Freire, *J. Comput. Chem.*, 2014, **35**, 772–775.

24 A. N. Carneiro Neto, E. E. S. Teotonio, G. F. de Sá, H. F. Brito, J. Legendziewicz, L. D. Carlos, M. C. F. C. Felinto, P. Gawryszewska, R. T. Moura, R. L. Longo, W. M. Faustino and O. L. Malta, in *Handbook on the Physics and Chemistry of Rare Earths*, ed. J.-C. G. Bünzli and V. K. Pecharsky, Elsevier, 2019, vol. 56, pp. 55–162.

25 C. S. McCamy, *Color Res. Appl.*, 1992, **17**, 142–144.

26 (*a*) S. Li, G. Zhong, W. Zhu, F. Li, J. Pan, W. Huang and H. Tian, *J. Mater. Chem.*, 2005, **15**, 3221–3228; (*b*) G. Zucchi, T. Jeon, D. Tondelier, D. Aldakov, P. Thuery, M. Ephritikhine and B. Geffroy, *J. Mater. Chem.*, 2010, **20**, 2114–2120.

27 G.-L. Law, K.-L. Wong, H.-L. Tam, K.-W. Cheah and W.-T. Wong, *Inorg. Chem.*, 2009, **48**, 10492–10494.